REPORT DOCUMENTATION PAGE

Public Reporting burden for this collection of information is estimated to average 1 hour per response, including the time for reviewing instructions, searching existing data sources, gathering and maintaining the data needed, and completing and reviewing the collection of information. Send comment regarding this burden estimates or any other aspect of this collection of information, including suggestions for reducing this burden, to Washington Headquarters Services, Directorate for information Operations and Reports, 1215 Jefferson Davis Highway, Suite 1204, Arlington, VA 22202-4302, and to the Office of Management and Budget, Paperwork Reduction Project (0704-0188,) Washington, DC 20503.

1. AGENCY USE ONLY (Leave Blank)	2. REPORT DATE 4/25/2005	3. REPORT TYPE AND DATES COVERED 15 Sep 01 – 14 Sep 04

4. TITLE AND SUBTITLE
1.55 Vertical Cavity Surface Emitting Laser with Dielectric Mirrors

5. FUNDING NUMBERS
DAAD19-01-1-0756

6. AUTHOR(S)
Dr. F. Ren
Dr. S. J. Pearton

7. PERFORMING ORGANIZATION NAME(S) AND ADDRESS(ES)
University of Florida
Department of Chemical Engineering
317 CHE Bldg
Gainesville, FL 32611

8. PERFORMING ORGANIZATION REPORT NUMBER
UPN:01051191

9. SPONSORING / MONITORING AGENCY NAME(S) AND ADDRESS(ES)

U. S. Army Research Office
P.O. Box 12211
Research Triangle Park, NC 27709-2211

10. SPONSORING / MONITORING AGENCY REPORT NUMBER

42831.3-EL

11. SUPPLEMENTARY NOTES
The views, opinions and/or findings contained in this report are those of the author(s) and should not be construed as an official Department of the Army position, policy or decision, unless so designated by other documentation.

12 a. DISTRIBUTION / AVAILABILITY STATEMENT

Approved for public release; distribution unlimited.

12 b. DISTRIBUTION CODE

13. ABSTRACT (Maximum 200 words)

Design, processing and characterization of high-speed implanted-apertured, lateral-current-injection, dielectric-mirror vertical cavity surface emitting laser and InGaAs based MEM detectors and mixers. We have achieved following goals:

I. Designed 1.55 micron InP/InGaAs based tunnel junction structure and purchased two samples with good quality. The VCSEL is being processed.

II. Designed SiO_2/TiO_2 based top and bottom DBR mirrors.

III. Performed the thermal simulation of flip-chip double-side dielectric DBR mirror VCSEL.

IV. Collaborated with Keith Aliberti and Paul Shen in ARL to fabricate InGaAs based MSM detectors and mixer.

V. Simulation of Pulse and DC Responses for Schottky Barrier Enhanced InGaAs MSM Photo-Detectors And OE Mixers

VI. Developed Submicron Inter-Digitated Finger Process To Reduce the Device Capacitance And Dark Current

VII. Working with ARL To Redesign the MSM Array Mask To Reduce Device Parasitic Capacitances

14. SUBJECT TERMS
Dielectric Mirror, Thermal Simulation, Resistance Simulation, Mask Design

15. NUMBER OF PAGES

16. PRICE CODE

17. SECURITY CLASSIFICATION OR REPORT UNCLASSIFIED	18. SECURITY CLASSIFICATION ON THIS PAGE UNCLASSIFIED	19. SECURITY CLASSIFICATION OF ABSTRACT UNCLASSIFIED	20. LIMITATION OF ABSTRACT UL

NSN 7540-01-280-5500

Standard
Form 298 (Rev.2-89)
Prescribed by ANSI Std. 239-18

Final Report of 1.55 Vertical Cavity Surface Emitting Laser with Dielectric Mirrors

Submitted by Fan Ren
University of Florida
Department of Chemical Engineering
Gainesville, FL 32611
Tel: (352) 392-4727
Fax: (352) 392-3235
Email: ren@che.ufl.edu

Stephen J. Pearton
University of Florida
Department of Materials Science And Engineering
Gainesville, FL 32611
Tel: (352) 846-1086
Fax: (352) 846-1181
Email: spear@mse.ufl.edu

Summary of Fianl Report

We have achieved following goals:

I. Designed 1.55 micron InP/InGaAs based tunnel junction structure and purchased two samples with good quality. The VCSEL is being processed.
II. Designed SiO_2/TiO_2 based top and bottom DBR mirrors.
III. Performed the thermal simulation of flip-chip double-side dielectric DBR mirror VCSEL.
IV. Collaborated with Keith Aliberti and Paul Shen in ARL to fabricate InGaAs based MSM detectors and mixer.
V. Simulation of Pulse and DC Responses for Schottky Barrier Enhanced InGaAs MSM Photo-Detectors And OE Mixers
VI. Developed Submicron Inter-Digitated Finger Process To Reduce the Device Capacitance And Dark Current
VII. Working with ARL To Redesign the MSM Array Mask To Reduce Device Parasitic Capacitances

I. Epitaxial Design

A tunneling junction based 1.55 µm VCSEL were designed and two samples were grown with MBE on InP substrate. The detail layer structure is illustrated in Table I.

Table I. Layer structure of 1.55 µm VCSEL.

Layer	Material	Description	Specs
Cladding	InP	Thickness	2.325um
		Doping	5×10^{18} cm^{-3} Si on top 10 nm, 5×10^{17} cm^{-3} Si for the rest of the film
Tunnel Junction	n^{++}InP	Thickness	20nm
		Doping	3×10^{19} cm^{-3} Si
	p^{++}InAlAs	Thickness	20nm
		Doping	1×10^{20} cm^{-3} C
QWs (Five Periods)	Al$_{0.08}$Ga$_{0.22}$In$_{0.70}$As	Thickness	70Å compressively strained QWs
	Al$_{0.15}$Ga$_{0.40}$In$_{0.45}$As	Thickness	50Å tensile strain barriers
Etch Stop	In$_{0.52}$Al$_{0.48}$As	Thickness	500Å

The proposed device structure is shown in Figure 1. The VCSEL fabrication starts with front side fabrication, then, the VCSEL will be flip-chip bond on carrier. The InP substrate is 20 mil thick and will be lapped down to around 4

mil. HCl will be used to etch off the rest InP and stop on InAlAs layer. The etch selectivity is around a few hundreds.
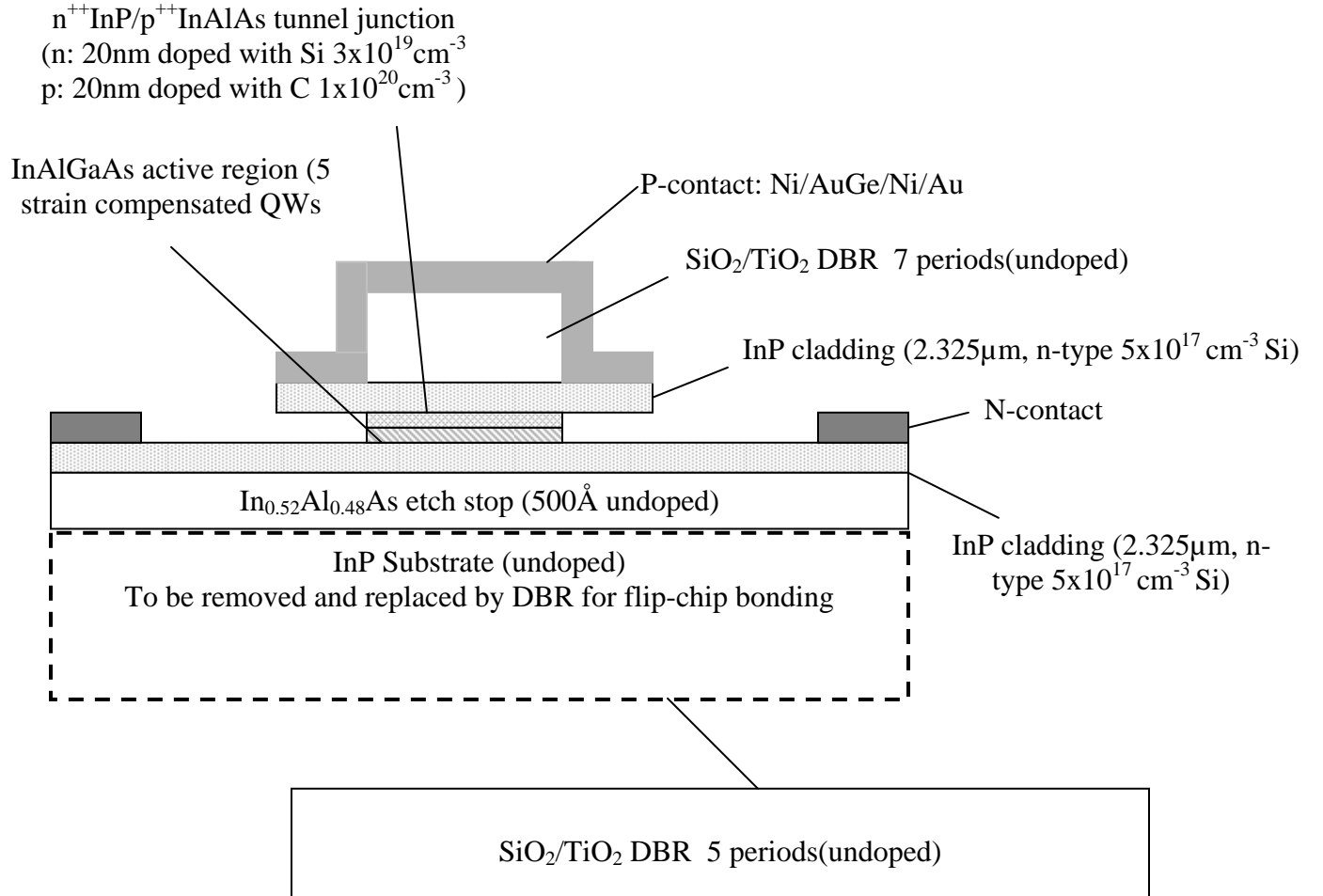
n^{++}InP/p^{++}InAlAs tunnel junction
(n: 20nm doped with Si 3x10^{19}cm^{-3}
p: 20nm doped with C 1x10^{20}cm^{-3})

InAlGaAs active region (5 strain compensated QWs

P-contact: Ni/AuGe/Ni/Au

SiO$_2$/TiO$_2$ DBR 7 periods(undoped)

InP cladding (2.325µm, n-type 5x10^{17} cm^{-3} Si)

N-contact

In$_{0.52}$Al$_{0.48}$As etch stop (500Å undoped)

InP Substrate (undoped)
To be removed and replaced by DBR for flip-chip bonding

InP cladding (2.325µm, n-type 5x10^{17} cm^{-3} Si)

SiO$_2$/TiO$_2$ DBR 5 periods(undoped)

Figure 1. Proposed 1.55 VCSEL layer structure and device configuration.

The room temperature PL shows a clear peak at 1.55 micron and low temperature PLs were also obtained, as shown in Figure 2. The intensity increased five times as measured at 16 K. AFM was used to measure the smoothness of the epi-sample. A root mean square roughness (RMSR) of 1.8 nm for a area of 5×5 µm^2 area was obtained as shown in Figure 3.
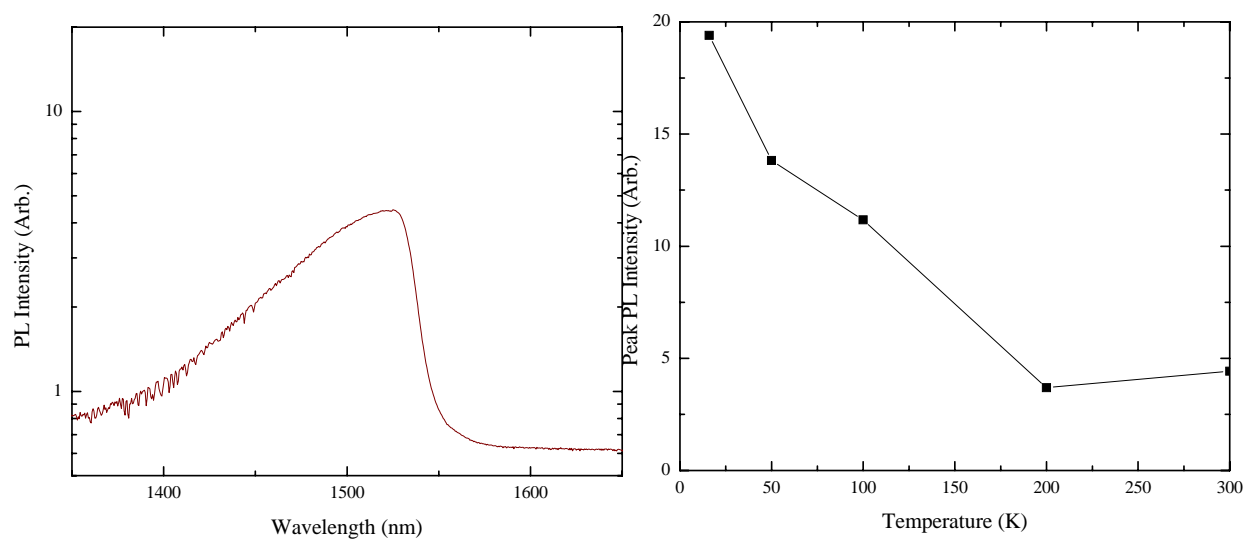
Figure 2. (Left) Room temperature PL of 1.55 micron VCSEL sample. (Right) Relative
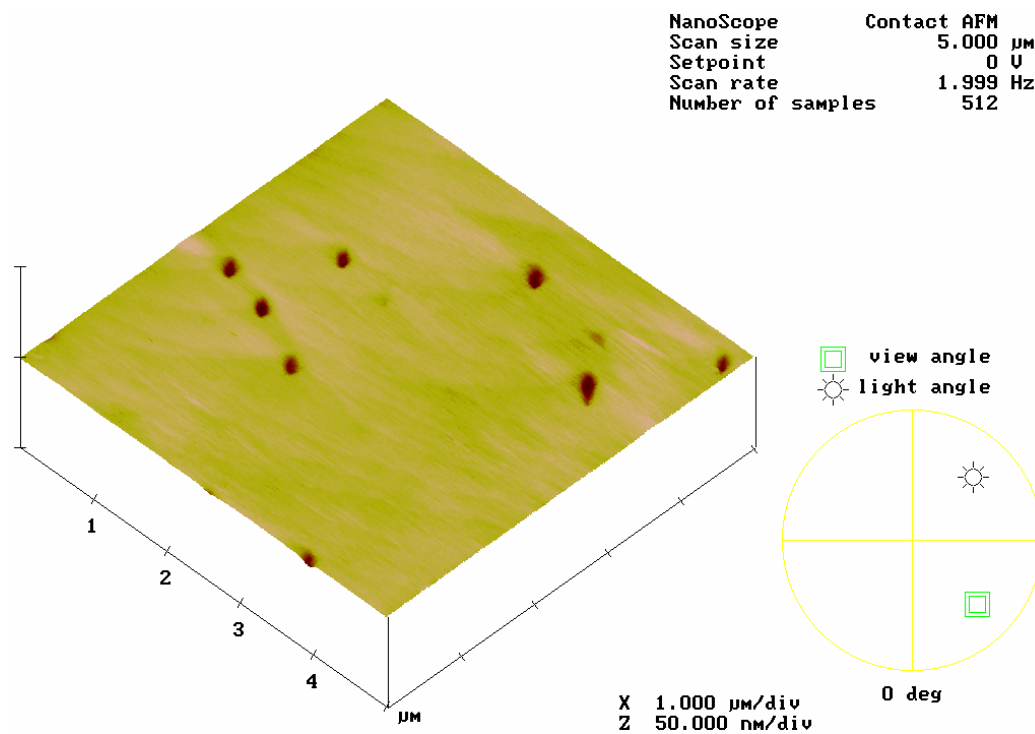PL intensity as a function of measurement temperature.

Figure 3. AFM of a 5×5 µm^2 area for MBE grown 1.55 micron VCSEL sample.

II. **Dielectric Mirror Design**

In InP based material system, high number of mirror pairs are needed due to the small difference in refractive indices between the high bandgap InAlAs and the low bandgap AlGaInAs resulting in a hugh layer thickness of more than 8 micron. We use SiO_2/TiO_2 dielectric DBRs to simplify the growth of VCSEL structure opening up the possibility of large-scale production. Fewer periods of dielectric mirror would achieve the desired reflectivity when compared to semiconductor mirrors.

The simulated of SiO_2/TiO_2 DBR reflectivity of the top and bottom mirror are shown in Figure 3. Top dielectric mirror consists of 7 periods of SiO_2/TiO_2 DBR with reflectivity of 99.96%. The bottom mirror can be deposited after flip-chip bonding the device to the heat sink and it consists of 5 periods of SiO_2/TiO_2 DBR with reflectivity of 99.59%.
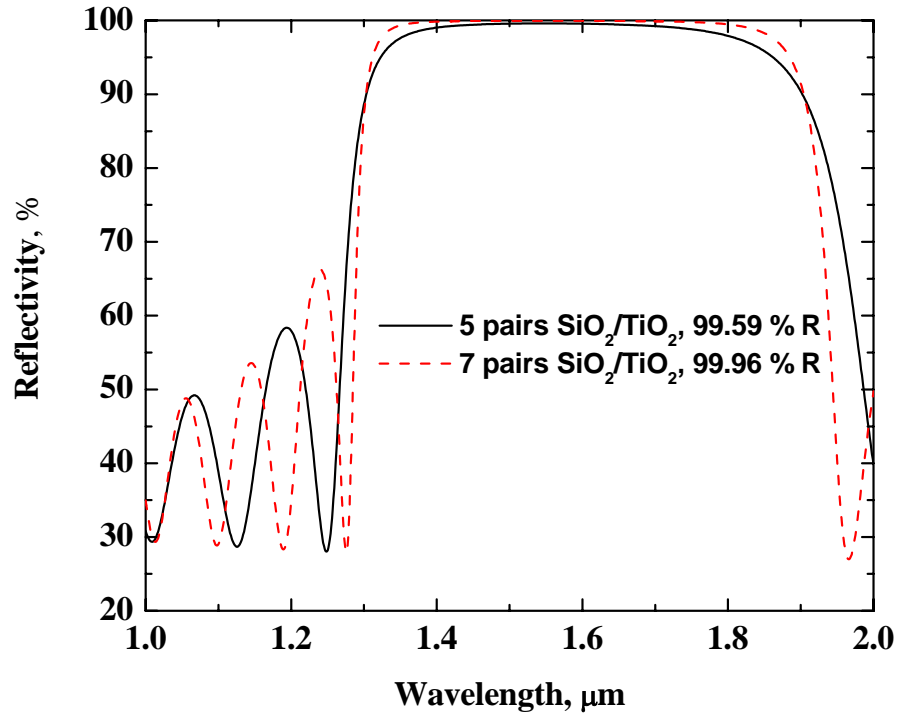
Figure 4. Simulated of SiO_2/TiO_2 DBR reflectivity of the top and bottom mirror.

III. Thermal Simulation

Figure 5 shows the heat flow vector –k(gradT) (on left) and constant temperature contours (on right) distribution across the cross-section of the VCSEL structure. Most of the heat flows into the heat sinks through the flip-chip bonded final metal bonding pads. Flip-chip bonding along with high electron mobility of InP also allows for the use of

lower doping concentrations without compromising high current injection level in the device. Further free-carrier absorption can be reduced by using low doping levels for InP layers.
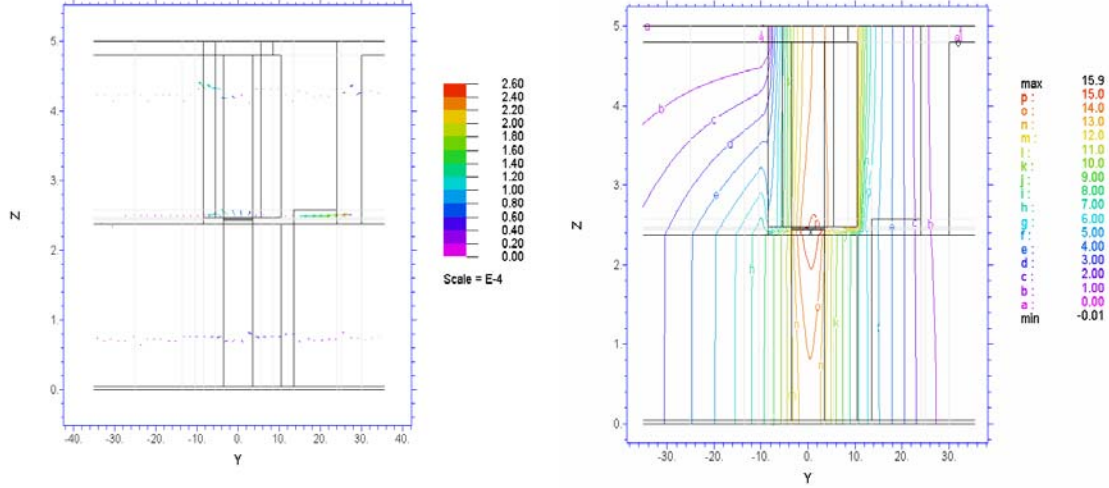

Figure 5. Heat flow vector on left and constant temperature contour on right across cross section of VCSEL.

The main heat generation, (70%) in the device occurs through Joule heating due to the resistance of semiconductor layers. Joule heating is given by $w(r, z) = \rho(r, z)j^2(r, z)$ where j is the current density flowing in the device and ρ is the electrical resistivity of the materials for the VCSEL layers. A resistance model (as shown in Fig. 6) was developed and the resistance for each epi-layer was estimated. Table 2. enlists thickness, doping, and calculated electrical resistance for each layer.
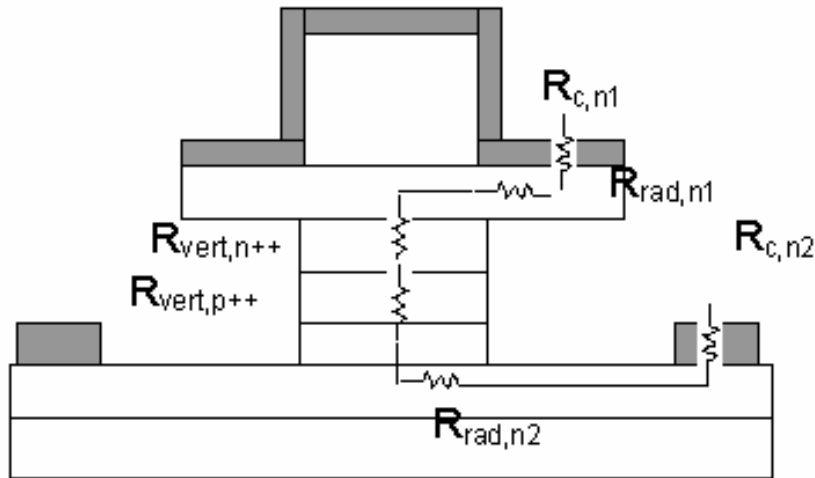
Figure 6. A resistance model of 1.55 mcron VCSEL for estimating the resistance of each epi-layer.

Table 2. Compilation of calculated resistances in VCSEL structure.

Layer	Thickness	Doping	R (Ω)
In P top	2.325 µm	5.00E+17	3.34
n++ InP	20 nm	3.00E+18	1.35×10^{-2}
p++ InAlAs	20 nm	1.00E+19	1.02×10^{-1}
InP bottom	2.325 µm	5.00E+17	7.60

This is intuitive since the resistance model would not account for any losses which might occur in the active region. 27% of the heat was generated by non-radiative recombination in the active region using their curve. Non-radiative recombination is governed by Auger recombination and Shockley-Read-Hall recombination. This portion of the heat generation was determined from the measured LIV characteristics of the laser diode and the estimated Joule heat generations. This modeling is based on the typical equation of energy for cartesian coordinates (x-, y- and z- axes),

$$\rho_{\underline{d}} C_p \frac{\partial T}{\partial t} - k \left[\frac{\partial^2 T}{\partial x^2} + \frac{\partial^2 T}{\partial y^2} + \frac{\partial^2 T}{\partial z^2} \right] = \frac{J^2}{\sigma} \qquad (1)$$

where t is time, ρ_d is density, C_p is heat capacity, J is current density [$A/\mu m^2$], k is thermal conductivity [$W/\mu m \cdot K$], and σ is electrical conductivity[$1/\Omega \cdot \mu m$] of each layer. The term on the right side of equation (1) corresponds to heat generation quantity per unit volume [$W/\mu m^3$]. The quantity of heat generation varies depending on specific regions and layers since current density and conductivity are functions of doping, composition and geometry of the device. The device dimension and temperature range considered in our case are very small, therefore, it is reasonable to assume the heat transfer through heat convection can be ignored. Three-dimensional temperature-distribution of VCSELs with flip-chip bonding is illustrated in Figure 7. The maximum temperature rise is 15.9 °C for the flip-chip bonded VCSEL The flip-chip bonded structure the top surfaces of final contact metal have been assumed to be at heat sink temperature. The maximum temperature occurred in the core of the active region in the VCSEL because the heat generation per unit volume is at its maximum in the active region layer. The excellent thermal characteristics of InP further helps rapid heat dissipation to the heat sink.

Figure 8. shows the effect of various current injection levels and the active region radius on the maximum temperature rise in the flip-chip bonded VCSEL. The temperature rise is almost linear at higher current injection levels (8 to 10 mA) in flip-chip bonded device, indicating the enhanced efficiency of heat dissipation in a flip-chip

bonded design. The maximum temperature rise decreases with increasing active region diameter, but the effect is not that significant in a flip-chip bonded VCSEL.
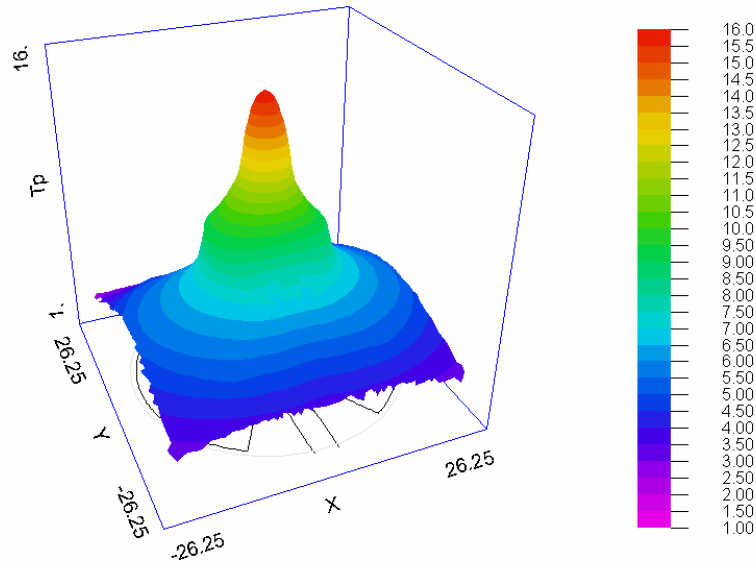

Figure 7. Three-dimensional temperature-distribution of VCSELs with flip-chip bonding.
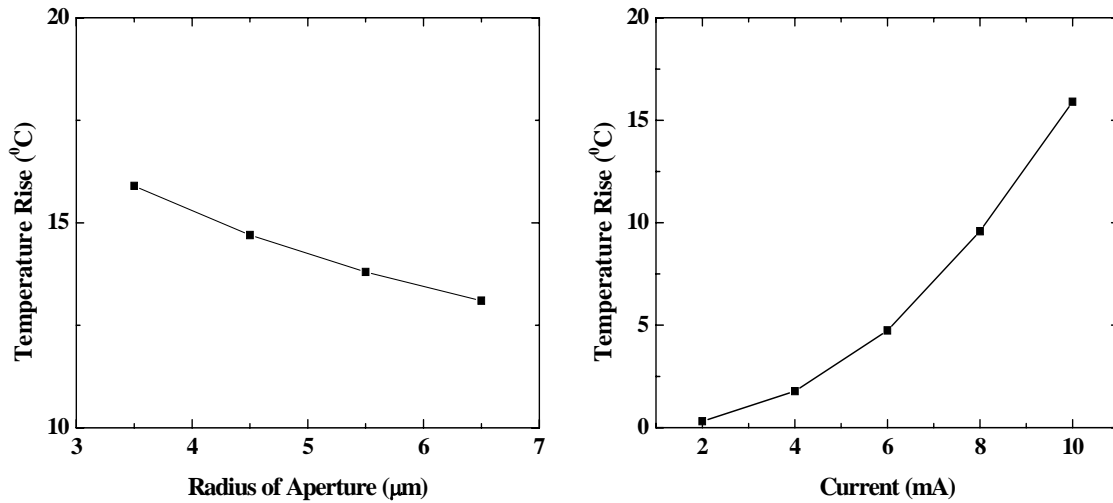

Figure 8 Effect of various current injection levels and the active region radius on the maximum temperature rise in the flip-chip bonded VCSEL.

To investigate the temperature rise when device is turning on, a dynamical model was investigated. Figure 9 shows the transient characteristics of the device when the current is switched on from 0 to 10 mA. The time needed for the device to reach the steady-state temperature was in the range of tens of microseconds, which is orders of magnitude larger than the electrical or optical switch time.
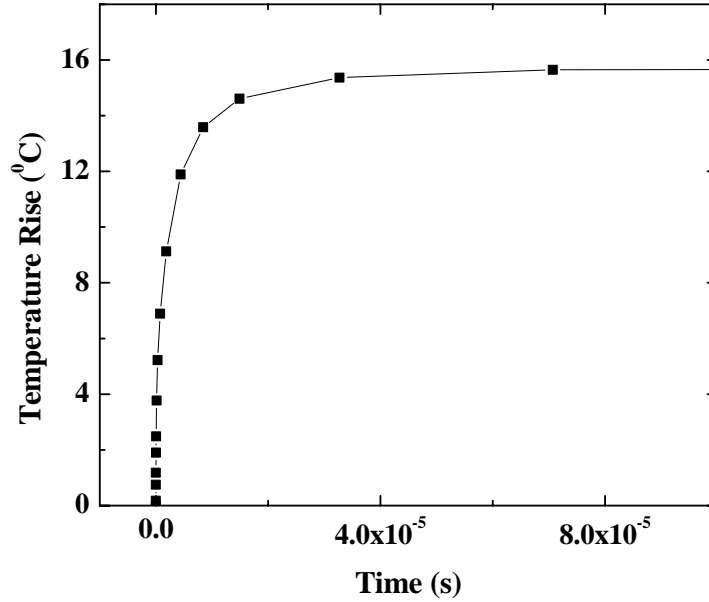

Figure 9. Transient characteristics of the VCSEL when the current is switched on from 0 to 10 mA.

IV. MSM Detector Fabrication

A comparison of various processing schemes for MSM InGaAs/InAlAs photodetectors on InP substrates with very low dark current and very high speed was conducted. Our metal-semiconductor-metal (MSM) structure consists of a 500-Å InAlAs/InGaAs multi-quantum well Schottky barrier enhancement layer, a 150-Å In(Ga,Al)As graded layer, a 1.0-μm InGaAs active layer, and a 0.3-μm InAlAs buffer layer grown on a semi-insulating InP:Fe substrate with a molecular-beam epitaxy (MBE) system. All devices were made using standard optical lithography and e-beam deposited Ti/Au metallization was used for Schottky and final metal contacts. Plasma enhanced chemical vapor deposited SiN_x and SiO_2 were employed for device passivation. CF_4/O_2 based plasma and H_2SO_4/H_2O_2/H_2O based wet-chemical etchant were used for dielectric etching and mesa definition.

Room temperature dark current measurements were performed using an HP4145B parameter analyzer. High speed measurements were conducted with a mode-locked Ti-sapphire laser-pumped optical parametric oscillator delivering 1.3-1.55-μm optical pulses

at 76-MHz and power was tunable to 3-nJ. The pulses passed through a continuously variable inline attenuator for power control and a beam splitter for power monitoring and the pulses were focused onto the device using a lens and a precision-adjustment stage. The high-speed signal was measured via two dc-to-40-GHz ground-signal-ground microwave probes attached through short transmission lines to a 40-GHz-digitizing oscilloscope.

To achieve very low dark current, high speed and high responsive goal, three different processing schemes were employed. In all of the processing schemes, the final metal contact pads were deposited on the top of a dielectric layer to reduce leakage current and capacitance resulting from the relatively large area of the final metal contact pads as compared to the actual device area. High leakage current means high dark current (high noise) and high capacitance means slower RC response in high frequency applications.

In the first MSM process scheme, Ti/Au (200Å/1800Å) based Schottky MSM fingers and finger-connections were deposited on top of the InGaAs/InAlAs MQW, followed by 1000 Å of Si_3N_4 and then 1850Å of SiO_2. The thickness of dielectric films was determined through a simulation so as to have reflection losses of less than 5% in the wavelength of interest. Then a contact window was opened in the dielectric layer to contact the metal finger-connections as shown in Figure 10(left). The Ti/Au (200Å/2500Å) based final metal contact pads connected the MSM Schottky fingers through the dielectric window. In this process scheme, the dark current was generated from the MSM Schottky fingers as well as metal finger-connections. The second scheme, as shown in Figure 1(right), employed a dielectric window. The metal finger-connections and finger-tips sit on the top of dielectric film. We opened the mesa window in the dielectric film (which was 2600 Å of Si_3N_4) by dry etch and wet etch in succession. The final few 100 Å of dielectric was removed by wet etch to avoid any plasma damage.
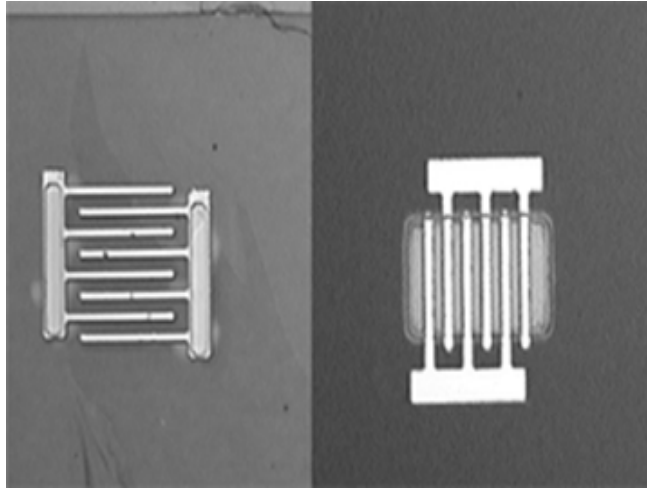

Figure 10. Photomicrographs of devices in which the contact window was opened after Schottky metal deposition (left) and in which the mesa was opened in the dielectric before putting down Schottky metal (right).

Dark current measurements were performed to determine the efficiency of each design in reducing noise. The measurements showed that the second processing scheme was more efficient in reducing the dark current. Dark current of less than 0.1 nA at a bias of 1V was obtained, as shown in the current-voltage(I-V) characteristics of Figure 11. By shape contrast, the dark current with the first processing scheme was on the order of 60 nA for a device of length 30 µm, finger width 1 µm and finger spacing 3 µm. In the second processing sequence, since the contact finger-tips were lying on top of the dielectric film, the dark current was greatly reduced. The electric field was also much more concentrated on the tip resulting in large leakage in the first case. This was further proven for measurements on a few devices in which their Schottky level was misaligned. The tips for these devices were on the semiconductor surface instead of the dielectric surface. These photodetctors displayed dark currents on the order of few 10's of nano Amps. There was also an increase in the dark current with increase in device size as seen in Figure 11.
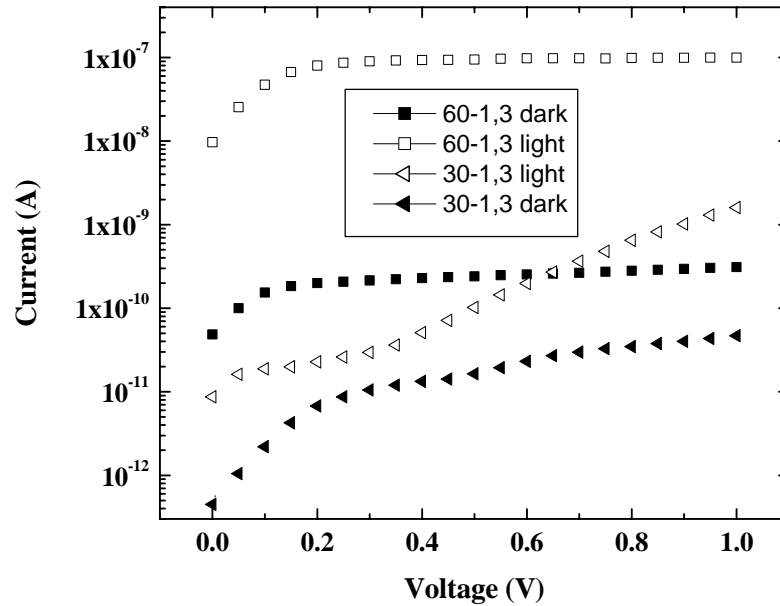
Figure 11. Measured I-V response of the device processed with the second type of fabrication sequence. The devices had lengths of 60 µm or 30 µm and finger widths of 1µm and finger spacing of 3 µm.

Figure 12 is a plot of the normalized temporal pulse response amplitude of these devices for three different biases. The device under test was a 50×50 MSM with 2.0-µm wide fingers with an inter-electrode spacing of 2.0 µm. The optical power on the sample was 0.36 pJ/pulse and $\lambda = 1.50$ µm. Table III gives the 10%-90% rise time, full width half maximum, and 10%-90% fall time for biases of 3.0 V, 6.0 V, and 9.0 V, respectively. Using the relation

$$f_{3dB} \cdot \tau_{10\%-90\%} = 0.35, \tag{2}$$

where $\tau_{10\%-90\%}$ is the measured rise time, the estimated 3-dB cutoff frequency f_{3dB} for 6.0 V was estimated as (i.e., the 3-dB bandwidth) ~22 GH. At 12V, we measured a rise time = 14.6 ps, FWHM = 40 ps, fall time = 129 ps and a 3 dB bandwidth of 24 GHz.
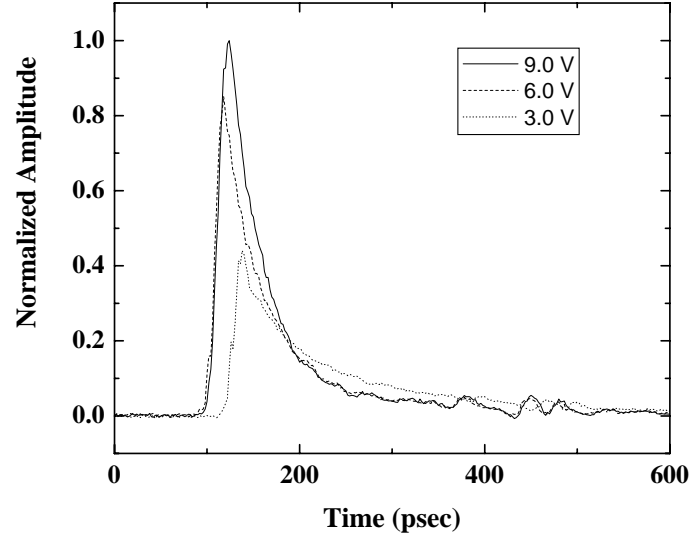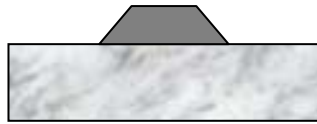

Figure 12. Temporal response for three different dc bias voltages for detectors processed with the second type of fabrication sequence.

Table III. Measured temporal response data for InGaAs MSM.

Bias	10%-90% rise time	10%-90% fall time	FWHM
3.0 V	16.5 ps	242 ps	54 ps
6.0 V	16.1 ps	119 ps	40 ps
9.0 V	18.0 ps	97 ps	41 ps

To further enhance the temporal response of the MSM detector without losing the advantage of low dark current, an etch back process was developed. Figure 13 shows the processing sequence to obtain a planarized structure before depositing the metal. The mesa was etched first, then a dielectric equal in height to this mesa was deposited using PECVD. Planarization of the dielectric film was achieved with a polymer coating and a planarization coating etch-back to expose dielectric top. Then, the etch chemistry was switched to etch the dielectric using the planarization coating as a mask to expose the top surface of the semiconductor. The planarization coating was subsequently removed with acetone at the completion of the process. Figure 14 illustrates a picture of a 30×30 μm^2 MSM etch-back device with 1.0-μm wide fingers and an inter-electrode spacing of 3.0 μm.
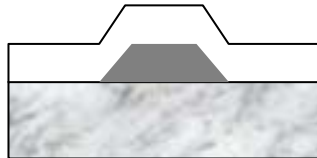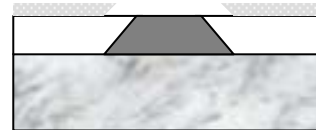
Mesa Etch

Planarizer
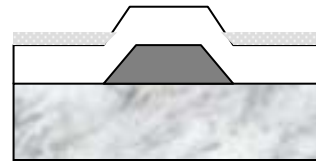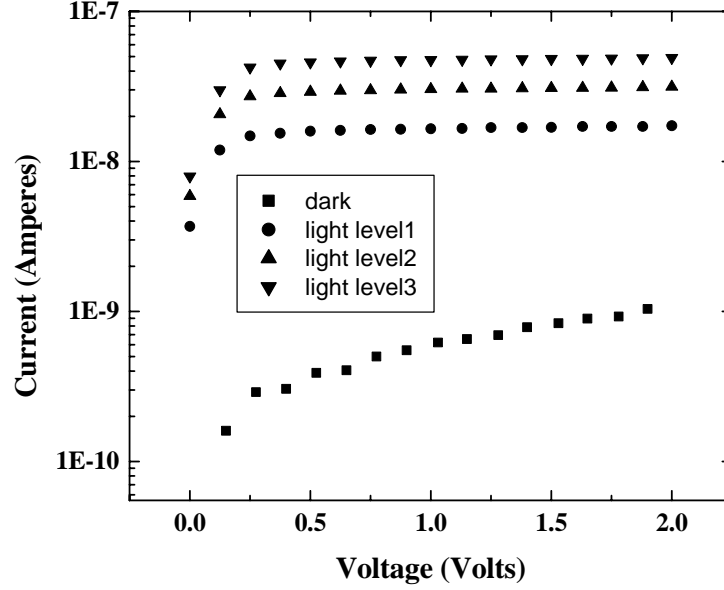
SiN$_X$

Oxide

Planarization

Planarizer

Figure 13. Processing sequence for etch back process

Figure 15 shows the dark current to be less than 1nA at 1V and the device to be highly linear in response to the different levels of microscope light. The dark current is slightly higher than for the second fabrication sequence, which may be resulted from the plasma etch damage during the etch back process. The damage can be reduced by switching the dry etch to wet chemical etching for the last few hundred angstroms of the dielectric film.
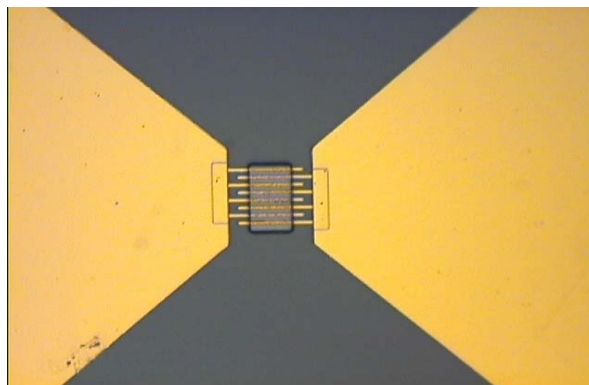
Figure 14. Top view of a 30 × 30 μm² MSM etch-back device with 1.0-μm wide fingers and an inter-electrode spacing of 3.0 μm.

Figure 15. Current -Voltage characteristic of a 30 × 30 μm² MSM etch back device with 1.0- m wide fingers with an inter-electrode spacing of 3.0 m

Interdigitated finger metal-semiconductor-metal photodetectors (MSMs) are widely used for high-speed optoelectronic (OE) applications and are also used as OE mixers to generate radio-frequency sub carriers in fiber-optic microwave links. InGaAs MSMs would allow LADAR operation at eye-safe wavelengths. Unfortunately, the Schottky barrier height on InGaAs is quite low (~0.1-0.2 eV) leading to high dark current and, hence, low signal-to-noise ratio. To reduce dark current, various methods of "enhancing" the Schottky barrier are used. The most promising method employs a high-band-gap lattice-matched InP [12] or InAlAs Schottky enhancement layer (SEL). Detectors using SELs yield low dark current, high responsivity, and high bandwidths.

We analyze the OE mixing effect in an InAlAs Schottky-enhanced InGaAs MSM detector. We show that the frequency bandwidth of such a mixer is less than that of a simple photodetector. We also show that the mixing efficiency (M_{eff}) depends on both the light modulation and IF frequencies and decreases non-linearly with optical power. We attribute this behavior to the band gap discontinuity associated with the SEL and present a circuit model of the OE mixer to explain the experimental results.

The MBE grown InGaAs MSM consists of a 500-Å InAlAs SEL, a 250-Å In(Ga,Al)As graded layer, a 1.0-μm InGaAs absorption layer, a 0.3-μm InAlAs buffer layer and a semi-insulating InP:Fe substrate. Ti/Au Schottky contacts were deposited by electron-beam evaporation with 3-μm finger widths and spacings. Contact pads and electrode tips were insulated from the InAlAs SEL to further reduce dark current.

Mixing characteristics were measured with light from an amplitude-modulated 1.55-µm, 10-Gb/s, fiber-pigtailed laser. Laser power was adjusted via a continuously variable, in-line, fiber-coupled attenuator. The LO bias was applied to one electrode, shunted with a 50 ohm termination, and the mixed signal was recovered from the other electrode which was connected to a spectrum analyzer through a low-pass filter.

Experimental Results

In Figure 16 we plot the IV characteristics of the MSM for optical powers of 7.0 µW and 0.722 mW. Both curves exhibit a region where dI/dV transitions from a low value to a high value: this is referred to as a "knee". InGaAs MSMs without SELs do not have any knee-like features. The knee voltage is the bias voltage where the photocurrent equals 5% of the value at the second region where dI/dV is low. The inset of Figure 16 shows the knee voltage as a function of the log of optical power.
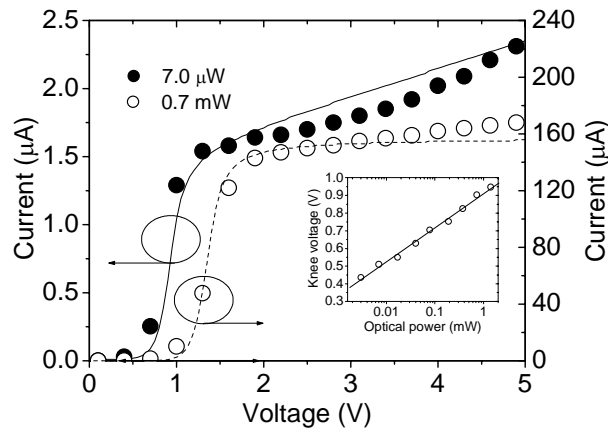

Figure 16. IV characteristics of InAlAs/InGaAs MSM for optical powers of 7.0 µW (solid circles) and 0.722 mW (open circles). Inset shows the knee voltage as a function of the log of optical power.

We define the mixing efficiency (M_{eff}) as the ratio of the responsivity at the IF frequency to its dc responsivity at the dc bias voltage equal to the RMS value of the ac voltage. Figure 17 shows M_{eff} as a function of laser modulation frequency for optical powers of 4.0-170 µW. Here, the modulation and LO frequencies were displaced by 10.0 KHz. M_{eff} is less than the theoretical value of 0.5 at low LO frequency and cuts off at about 0.1 GHz. Moreover, M_{eff} is optical power dependent: it increases with optical power and reaches the theoretical value at high optical powers. When the MSM is operated as a simple photodetector it has a flat frequency response with a 3.0-dB cut off at 3.0 GHz. In addition, the responsivity is independent of optical power except for powers above 4.0 mW where screening causes a slight decrease.
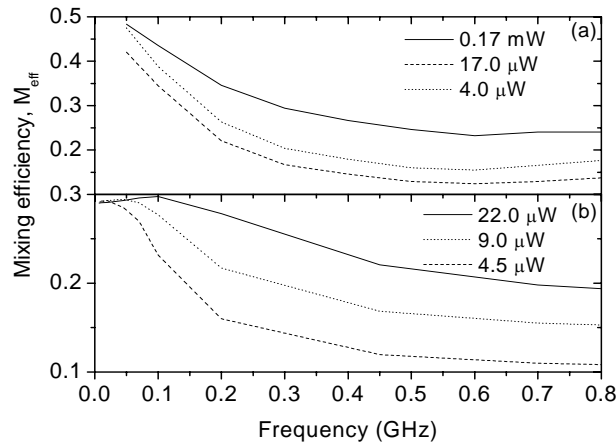
Figure 17 M_{eff} as a function of laser modulation frequency for optical powers of 4.0-170 μW.

Figure 18 shows M_{eff} as a function of IF frequency for optical powers of 17.0-140 μW. Here, the modulation frequency was at 500 MHz, while the LO frequency was varied from 500-715 MHz, yielding IF frequencies from 0-215 MHz. M_{eff} is flat with IF frequency to 10-30 MHz beyond which an increase occurs. At low IF frequencies, M_{eff} decreases as optical power decreases, while at high IF frequencies it approaches its theoretical value. We have compared the sum frequency with the difference frequency signal and found that the sum signal is independent of optical power and close to 0.5. In addition, the sum signal is larger than the difference signal. We would expect that, since the difference signal is at low frequency and the speed of a MSM is limited by the transient time and the circuit RC constant, an OE mixer would work better than or equal to a simple detector. Because this is true experimentally and theoretically for GaAs-based MSMs, but not for InAlAs/InGaAs-based MSMs indicates that low frequency signals are limited by some circuit component in the device.
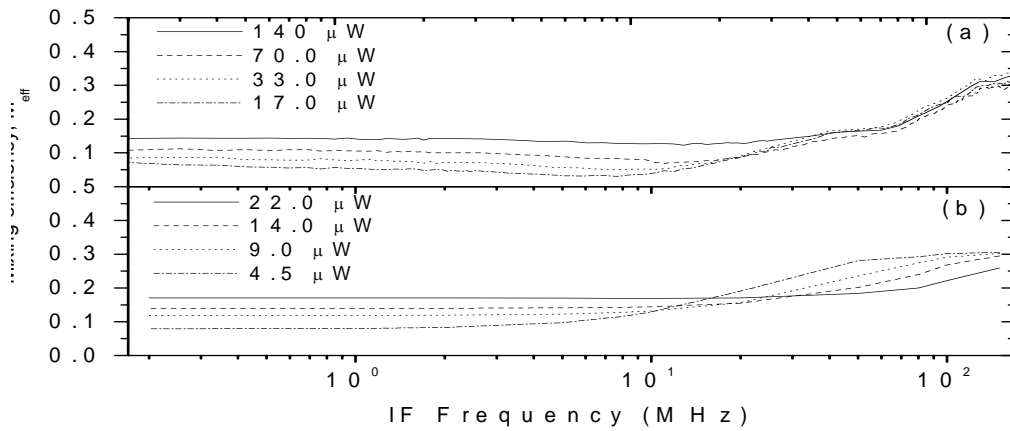

Figure 18 shows M_{eff} as a function of IF frequency for optical powers of 17.0-140 μW.

V. Two Dimensional Simulation of Pulse and DC Light Response As Well As Mixing Characteristics of Schottky Barrier Enhanced InGaAs MSM Photo-Detectors And OE Mixers

InGaAs based opto-electronic devices are becoming very important in many areas, such as telecommunications and imaging recognitions. High mobility, direct Band Gap and possibility of room temperature operation makes this material system very attractive to work with for wavelengths 1.30-1.55 μm. An understanding of device physics and accurate modeling of devices would help to develop better devices. Finite volume based simulations were performed for transient and DC response of the MSM photodetector. The simulation agreed the experiment results.

The simulations were carried out for a 60×60 μm^2 device with 3 μm finger width and 3 μm spacing between fingers. The physical properties of the InGaAs and InAlAs material systems used in our MSM detectors were not provided in CFDRC software, which is commercially available software and leased by UF. Matthiesen rule was used to estimate the mobility of InAlAs.

$$\frac{1}{\mu^{AB}} = \frac{x}{\mu^A} + \frac{1-x}{\mu^B} + \frac{x.(1-x)}{C_\mu}$$

where μ and x are mobility and mole fraction of corresponding species (InAs and AlAs, respectively) and C_μ is the bowing parameter. With the known mobility of the constituent semiconductors (InAs and AlAs) and the mole fraction of the Al in InAlAs, the mobility of the InAlAs was determined. For the InGaAs, a constant mobility of 12000 cm^2/V-s and 300 cm^2/V-s for electron and hole, respectively were used. The recombination life times of electrons and holes of $\tau_{electron} = 1\times10^{-9}$ s, $\tau_{hole} = 2\times10^{-8}$ s for InAlAs, respectively, and $\tau_{electron} = 1\times10^{-9}$ s, $\tau_{hole} = 1\times10^{-9}$ s for InGaAs, respectively.

a) Electromagnetic Simulation

Maxwell's equation was used to solve the magnetic potential vector, A, and electrostatic potential, ϕ.

$$\frac{1}{\mu_0\mu_r}\nabla^2\vec{A} = \varepsilon_0\varepsilon_r\frac{\partial^2\vec{A}}{\partial t^2} + \varepsilon_0\varepsilon_r\frac{\partial\nabla\phi}{\partial t} + \sigma\frac{\partial\vec{A}}{\partial t} + \sigma\nabla\phi - \sigma(\vec{u}\times\vec{B}) - \vec{J}_s$$

where B is the external magnetic field, u is the velocity of carriers, J_s is the current from any other source, μ_0 is the permeability of free space, μ_r is the relative permeability of the semiconductor respectively, ε_0 is the permittivity of free space, ε_r is the relative permittivity of the semiconductor, and σ is the conductivity of semiconductor.

Light intensity of the light source for the MSM detection, I, can be expressed as the modulus of a pointing vector, $\vec{S}$, and is also proportional to the square of the magnetic potential vector.

$$I = \left|\vec{S}\right| \propto \left|\vec{A}\right|^2$$

The power dissipation in each node can be determined by taking the divergence of the pointing vector. Then, the estimated power dissipation can be used to estimate the number of carriers generated in the semiconductor due to the fundamental absorption process.

Thus the continuity equation equations can be solved with the estimated carrier generation rate. The continuity equation is given by

$$q\frac{\partial n}{\partial t} + \nabla \vec{J}_n = q(G - R)$$

$$q\frac{\partial p}{\partial t} + \nabla \vec{J}_p = q(G - R)$$

where $\vec{J}_n$ and $\vec{J}_p$ are current electron and hole current densities respectively, n and p are the electron and hole densities respectively, q are the electronic charge, G is the generation rate of carriers and R is the recombination rate of carriers.

Python Script Modification

CFDRC has developed python script for data flow management and control of coupled electromagnetic optics/semiconductor physics simulation of MSM photodetector. The script was modified to include an extra SEL layer in the original MSM-photo detector simulation. The grid spacing was also changed to account for the width of the incorporated layer. Template files for the optical, steady state and transient simulation were modified to include boundary and volume conditions for the included layer. To create the new template files, the Python script was run to create a GEOM (GGD) files, for which template DTF files were created and boundary and volume conditions were manually assigned to these files.

Simulated Pulsed Responses

Figure 19 shows the spatial distribution of optical power dissipation, which was fed into the CFD-ACE+ SEMI module to solve for the pulsed responses of electron and hole after the removal of the light source. Figure 20 shows the electron and hole distribution just after the end of the light pulse and at two other time intervals from the removal of light pulse.
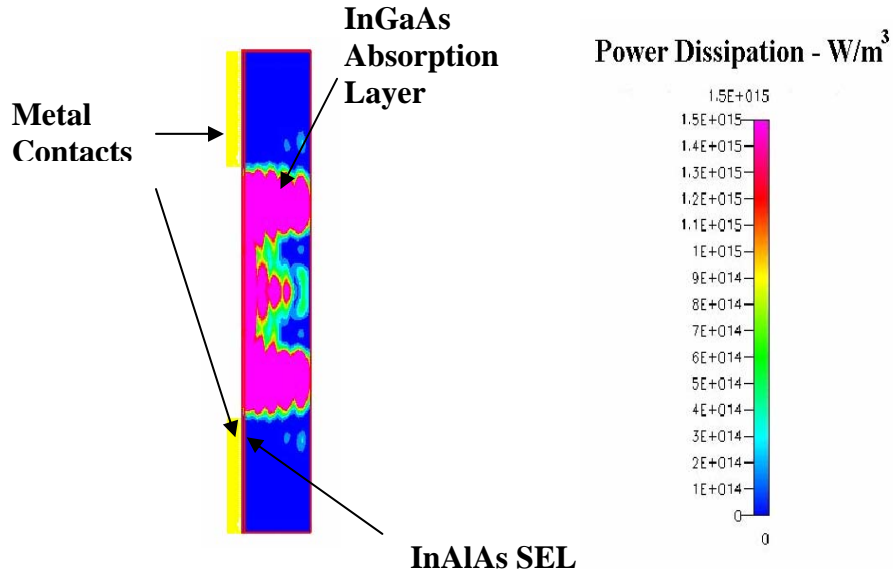
Figure 19. Simulated Power dissipation in the InAlAs/InGaAs MSM Detector.
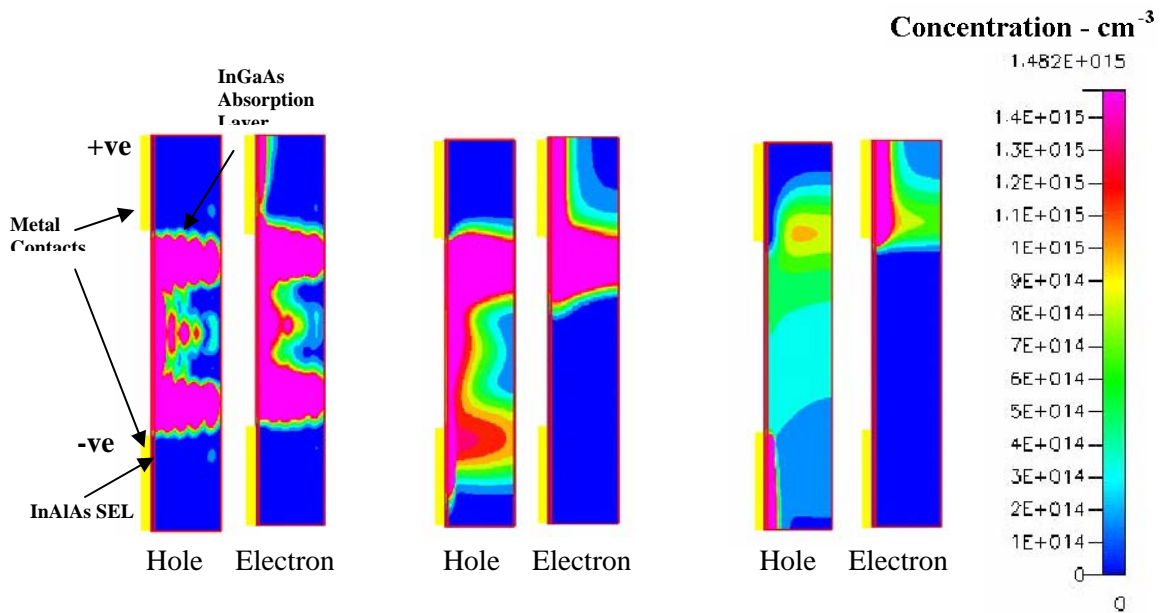

Figure 20. Electron and hole distributions at the end of the (left) 100 fs long light pulse (center) after 5ps from removal of light pulse (right) after 215 ps from removal of light pulse

It can be seen that electron and hole distributions follow the power dissipation profile very closely during the light exposure and right after the removal of the light. After the light pulse was switched off the carriers were swept away by the biases and terminated due to recombination. The recombination rates of the electron and hole were assumed the same, however, as shown in the Figure 20, the electron was quick swept to

the +-electrode due to the higher electron mobility. Hole mobility was the limiting factor for the MSM operation speed.

Original photo-detector simulation had the light pulse on for sufficient period of time (10 ps) and then switched off. This methodology could not be used for the transient simulation of the InGaAs MSM detector, due to short time period of the pulse (100 fs), which was incident on the detector. Instead, the transient simulations were divided into 3 different time period zones, depending on how fast the detector was switching. During the 100 fs time when the light was on the detector, a time period of 10 fs was used, during next 10^{-10} s, a time period of 10^{-12} s was used, and finally during last 9×10^{-10} s, a time period of 10^{-11}s, was used. This could be accomplished by using parametric input option in the time step and writing the time step and a total number of time steps=200.

Figure 21 shows the simulated and measured pulse response and the rise time of 14 ps and FWHM of 44 ps were obtained. The measured data gives rise time of 20 ps, and FWHM of 140 ps. The simulated results showed reasonable agreement with measured data.
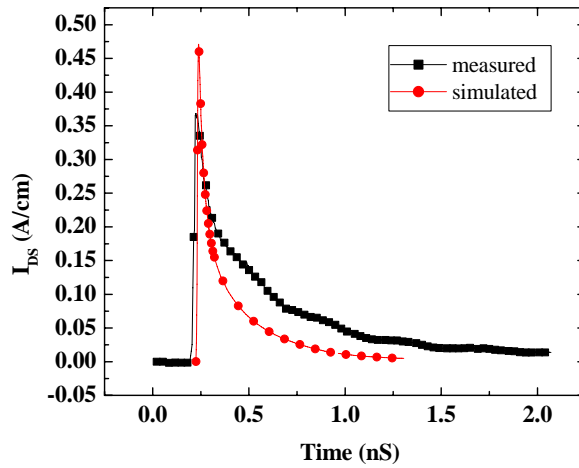

Figure 21. Pulsed response of MSM photo detector.

Simulated DC Responses

The simulation was setup for transient semiconductor simulation, with very long total time for photo-generation and the current converged to a constant value. When higher light intensity was simulated, time step had to be re-adjusted since the number of the carriers was very large.

Figure 22 shows the measured and simulated DC response of the MSM-photodetector under illumination with a 1.55 μm wavelength LASER. A good agreement between the simulated and measured I-V curves was obtained. The I-V curves exhibit a region where the slope of the I-V curve (dI/dV) transit from a low value to a high value. This transition is referred to as the knee voltage. This knee voltage is defined as the bias voltage at which the photocurrent equals 5% of the photocurrent at the second region where dI/dV is low.
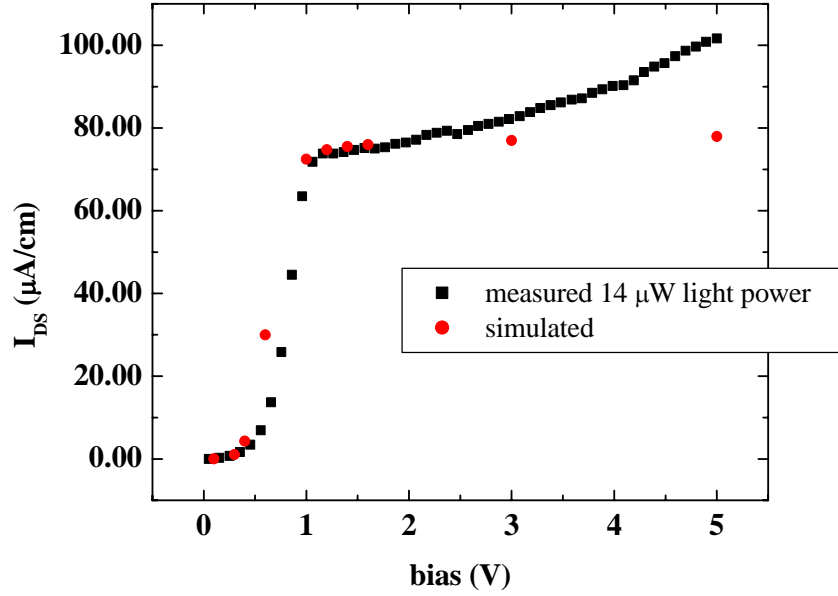
Figure 22. DC responsivity of a 60 μm × 60 μm MSM photo-detector with 3 μm finger width and 3 μm finger spacing.

The knee voltage of the I-V curve was due to the band discontinuity between InAlAs and InGaAs. As shown in Figure 23, our simulation predicted decrease in knee voltage with decrease of SEL thickness. As the thickness of SEL decreases, the tunneling current will increase and the knee would vanish altogether with SEL. The presence of 'knee' is also considered responsible for poor mixing efficiency of 500 Å SEL OE mixer. The MSM Photodetector's response as a function of light intensity was also simulated, as shown in the Figure 24, and similar trends were obtained. The decrease in mobility caused by increased carrier generation is responsible for the higher knee voltage. Knee voltage increases with increasing light intensity.
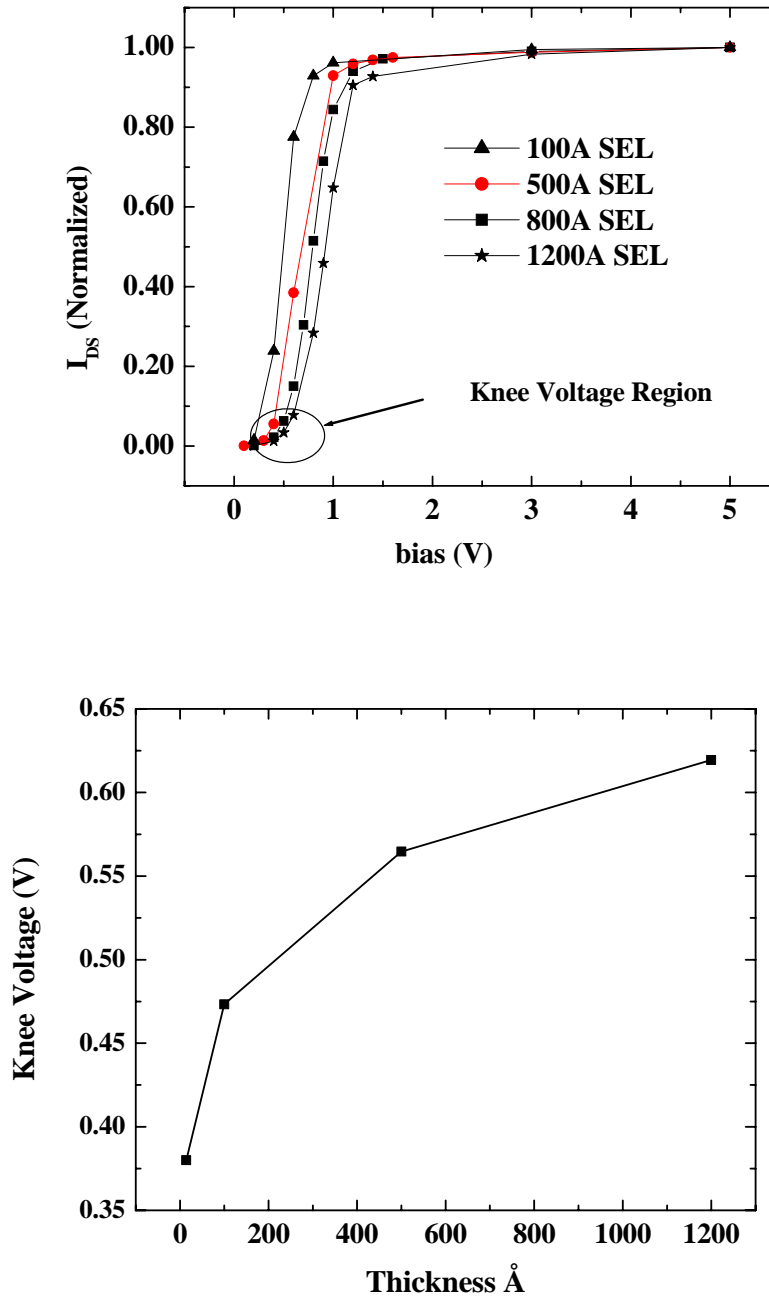
Figure 23. (top) Simulated DC responsivity of a 60 μm × 60 μm MSM photodetector with 3 μm finger width and 3 μm finger spacing for different SEL thicknesses at 14 μW of the light intensity. (bottom) Knee Voltage as a function of InAlAs layer SEL thickness.
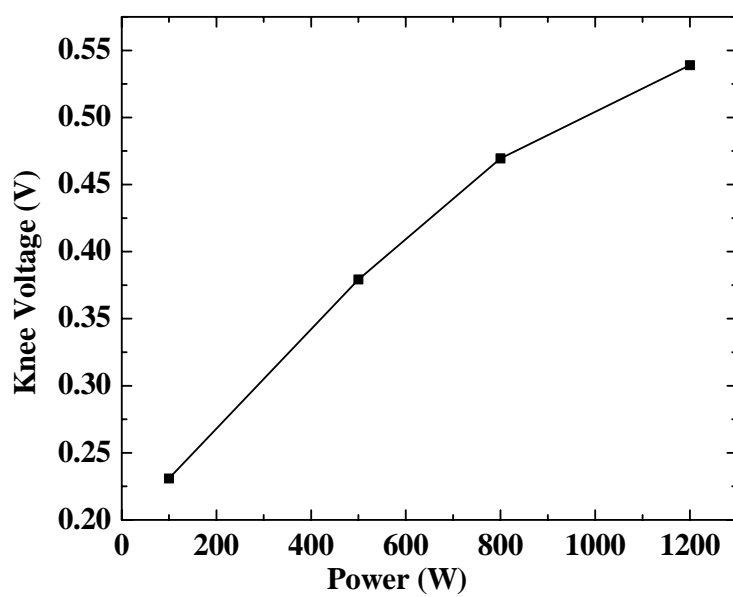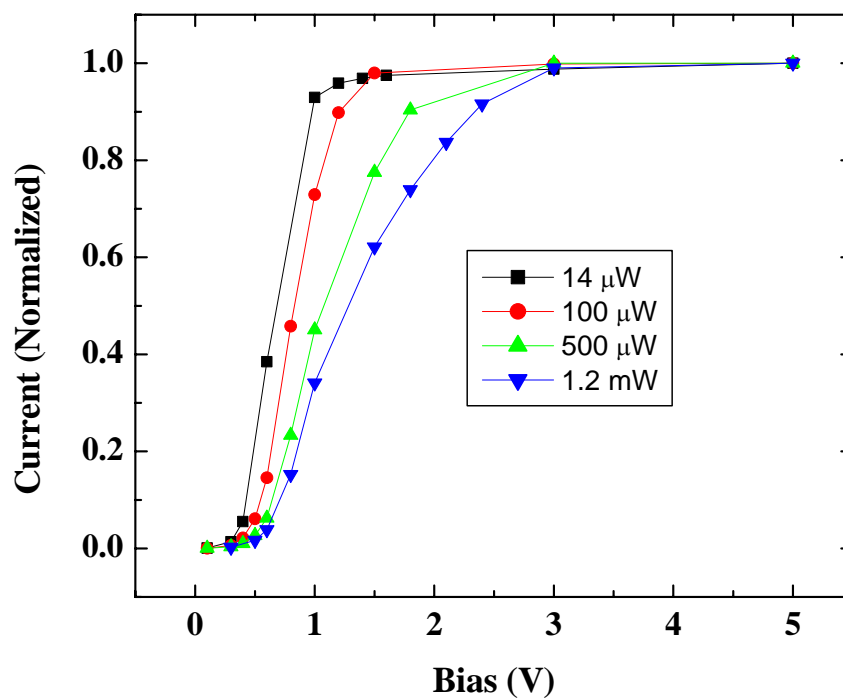
Figure 24. (top) Simulated DC response of InAlAs/InGaAs OE mixer for different light intensities. (bottom) Knee voltage as a function of power for 100 Å of InAlAs SEL.

VI. Developed Submicron Inter-Digitated Finger Process To Reduce the Device Capacitance And Dark Current

UF installed Raith-150 electron beam direct write system in 2003. The smallest beam spot size is 4 nm. PMMA based resist was used to pattern and form submicron inter-digitated fingers. Figure 25 shows a MSM device with 0.2 µm interdigitated finger.
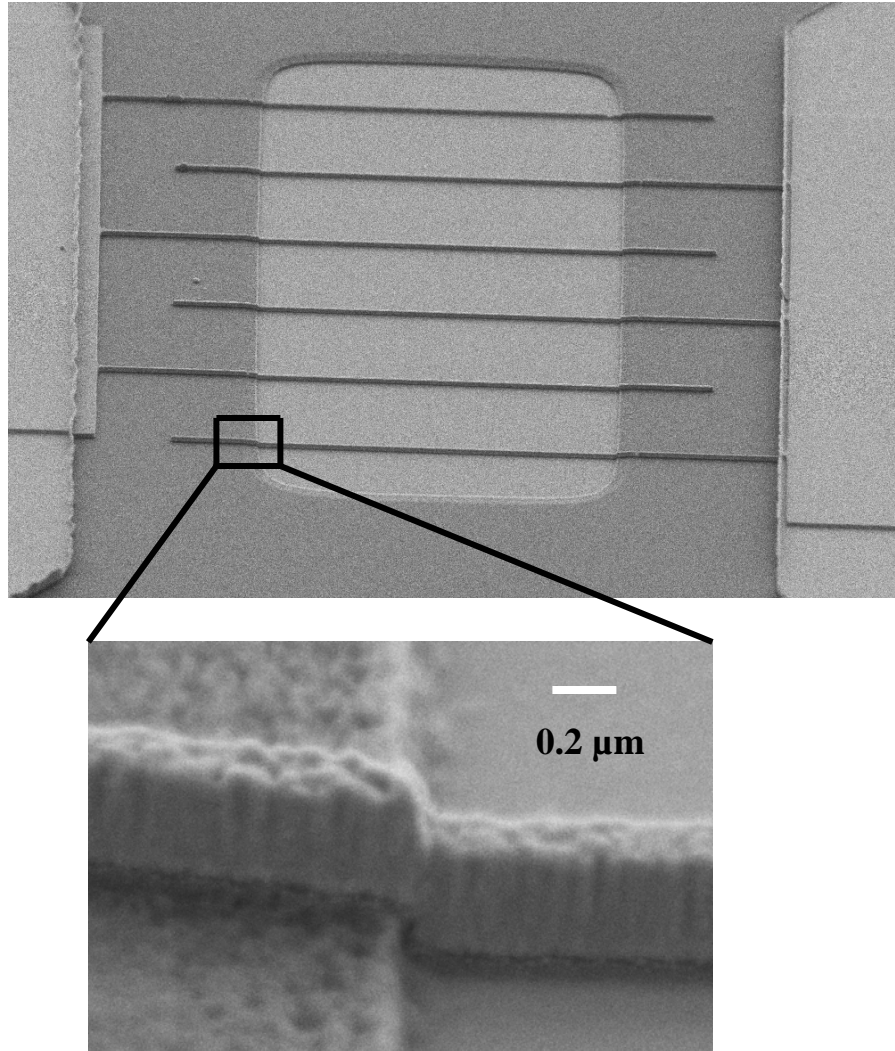

Figure 25. SEM of a MSM device with 0.2 micron width of inter-digitate Ti/Au fingers.

The dark current of the MSM device with submicron inter-digitate fingers is an order less than that of the MSM device with 1 micron wide fingers, as shown in Figure 26. Mushroom gate or T-gate device technology development was also developed to reduce the finger resistance. A tri-layer resist system consists of PMMA (2000 Å), PMMA-MAA copolymer (5000 Å), and PMMA (1200 Å), as shown in Figure 27. The top resist layer defines the periphery of the gate, whereas the bottom layer defines its

electrical contact. The PMMA-MAA middle layer is much more sensitive to the E-Beam radiation than the PMMA resist, so it develops much faster to give an overhanging structure crucial for lift-off processes. Forward scattering of electrons during E-Beam exposure step is very important for formation of the right kind of profile. Very large forward scattering will cause the bottom electrical contact of the gate to broaden.
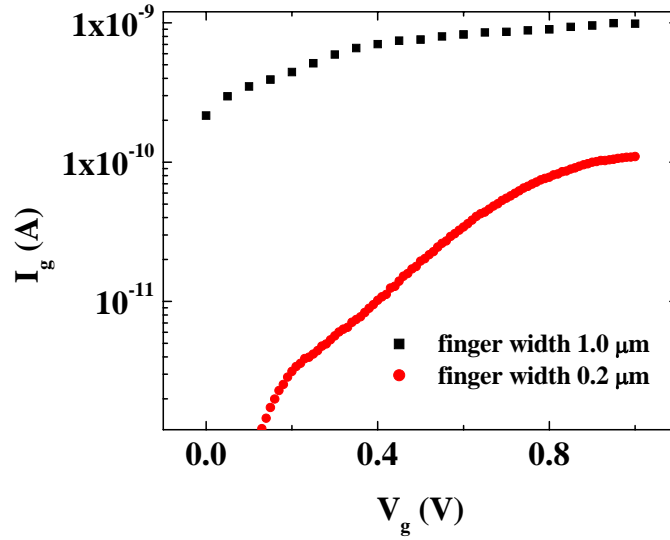

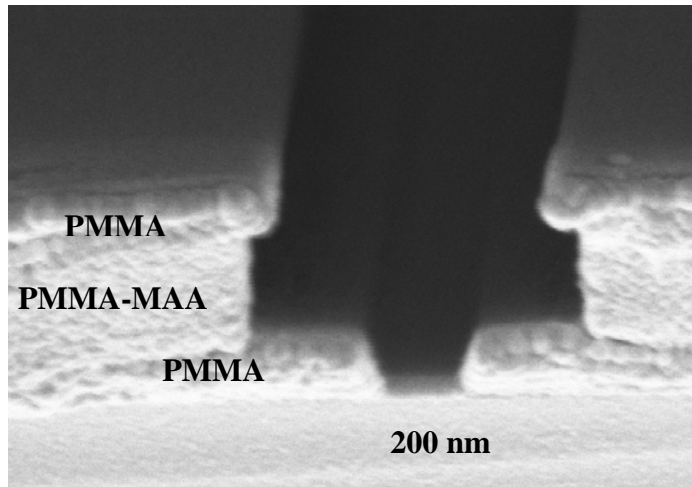Figure 26. Dark current of the MSM devices with 1.0 and 0.2 micron wide inter-digitated fingers.

Figure 27. Cross-sectional view of a tri-layer resist system developed in UF.

VII. Redesign the MSM Array Mask To Reduce Device Parasitic Capacitances

Working with scientists in Army Research Labs., a MSM array mask was redesigned. A mesa level was included to reduce the substrate capacitance. A dielectric

etch back process is under developing to improve the yield and uniformity of the MSM array. Figure 28 illustrates the modified device layout and a fabricated device.

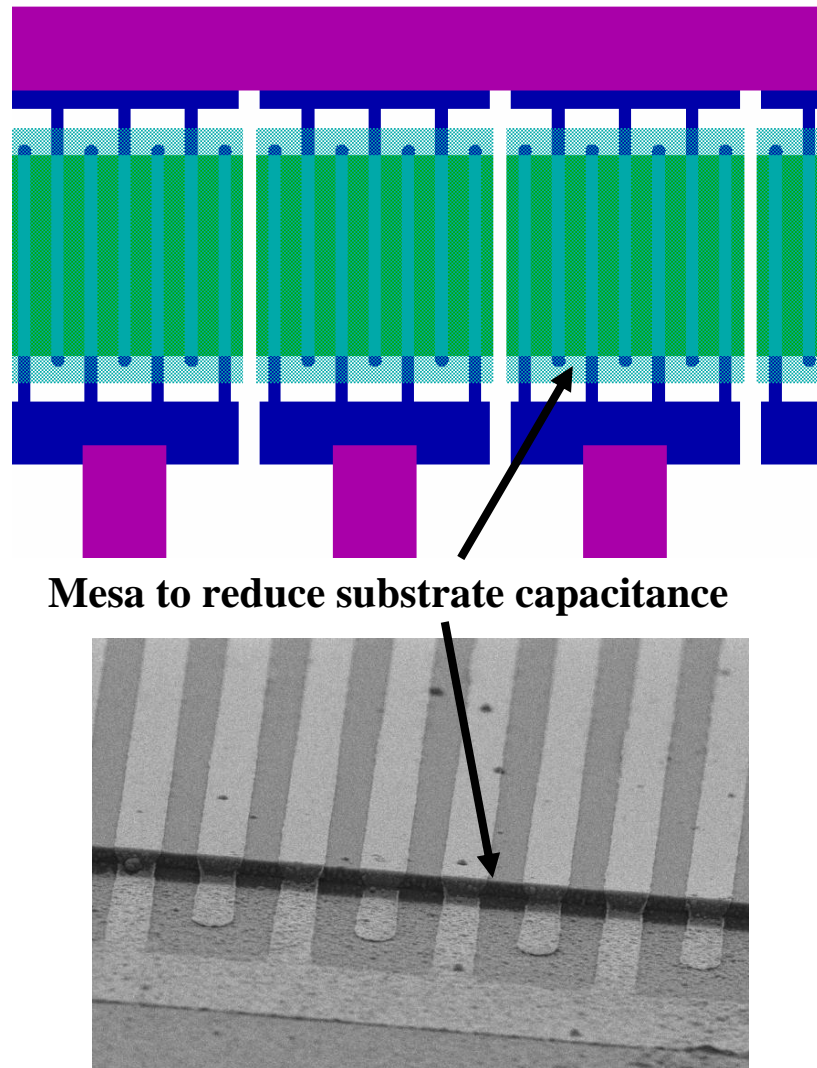**Mesa to reduce substrate capacitance**

Figure 28. (top) Layout of a MSM array with mesa level to reduce substrate capacitance. (bottom) SEM of a MSM with mesa.